



Visible light driven selective oxidation of amines to imines with BiOCl: Does oxygen vacancy concentration matter?

Chengliang Mao^a, Honggang Cheng^a, Hao Tian^b, Hao Li^a, Wen-Jing Xiao^a, Hu Xu^b, Jincai Zhao^a, Lizhi Zhang^{a,*}

^a Key Laboratory of Pesticide & Chemical Biology of Ministry of Education, Institute of Environmental & Applied Chemistry, College of Chemistry, Central China Normal University, Wuhan 430079, PR China

^b Department of Physics, South University of Science and Technology of China, Shenzhen 518055, PR China

ARTICLE INFO

Keywords:

Oxygen vacancies
Molecular oxygen activation
Bismuth oxychloride
Selective amines oxidation
Photocatalysis

ABSTRACT

The relationship between oxygen vacancy (OV) concentration of semiconductors and their photocatalytic performances is far from clarified. In this study, by tuning the OV concentration of BiOCl (001) surface via a novel H₂O₂ treatment coupled infrared irradiation method, we demonstrate that OV concentration of BiOCl (001) surface strongly determine its surface atomic and electronic structures to modulate the photocatalytic pathways. Being of shorter Bi–Bi and Bi–O bond lengths as well as more electrons being less localized, BiOCl (001) surface with higher OV concentration favored molecular oxygen activation to generate O₂^{2−} via a two-electron transfer pathway, while the generated O₂^{2−} could prevent the over oxidation of amines and thus achieve high selectivity in the oxidation of amines to imines. Similar phenomena were also observed for other semiconductor photocatalysts such as TiO₂ and Nb₂O₅, suggesting the generality of oxygen vacancy concentration mediated selectivity enhancement. These findings shed light on the relationship between the oxygen vacancy concentration and the surface structure of semiconductor photocatalysts and offer a novel pathway to realize photocatalytic selective oxidation of amines to imines.

1. Introduction

Surface oxygen vacancies (OVs) are the most reactive sites for small molecules activation on the surface of metal oxide photocatalysts, being of vital importance to wastewater remediation, artificial synthesis, nitrogen fixation and water oxidation with solar energy [1–8]. OVs possess excess localized electrons and coordinatively unsaturated nature, and thus provide specific sites to firmly bind small molecules, facilitating the subsequent molecules activation by photogenerated electrons injection [9–12]. Specially, such an activation process on OVs is dependent on the structure of OVs, generating different active species to participate in photoreactions on the surface. For example, our group demonstrated that OVs of BiOCl could activate molecular O₂ (~1.21 Å) to generate reactive oxygen species (ROS) like ·O₂[−] (~1.26 Å) or O₂^{2−} (~1.49 Å), and also activate molecular N₂ (~1.10 Å) to active nitrogen species of N≡N (~1.14 Å) or N=N (~1.20 Å), depending on the atomic and electronic structures of OVs [3,13]. Obviously, these different active species stemmed from distinct OV structures would strongly determine the pathways, products and rates of photocatalytic reactions [13–16]. Therefore, the OV structures tuning is a facile way to

precisely modulate the active species for desired reactions on the surface, which has been called as oxygen vacancy-mediated photocatalysis recently [6].

The most popular OV structure tuning method is to synthesize nanostructures with different facets, as the OV structures are usually determined by surface atomic structures of different facets [4,8–10]. Despite enormous advances in nanocrystals synthesis, this method still lacks the generality because of great challenges during the synthesis of photocatalysts exposed with specific facets for many metal oxides [17].

Besides the traditional facet exposure dependent OV structure tuning, changing the OV concentration of metal oxides' specific facets might be a facile pathway to tune the OV structures. This is because vicinal atoms of OV undergo distortion to minimize the free energy, and thus the OV concentration change can alter the distortion degree of these vicinal atoms, generating OVs with different atomic and electronic structures (Fig. 1). Obviously, this novel OV concentration mediated structure tuning method might be more promising, because OV engineering is applicable to all the metal oxide photocatalysts [18,19]. Although OVs are commonly regarded as the active sites in photocatalysis, the concentration of OVs is never associated with their

* Corresponding author.

E-mail address: zhanglz@mail.ccnu.edu.cn (L. Zhang).

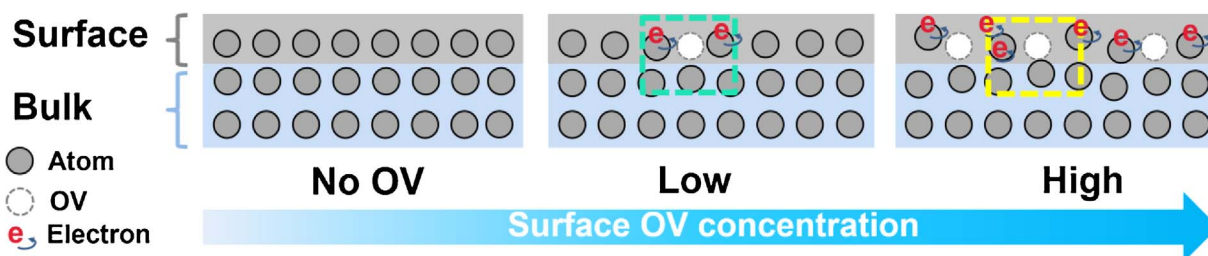
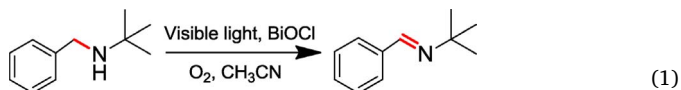


Fig. 1. Schematic illustration of OV concentration mediated surface structure change of metal oxides. Green and yellow boxes show the atomic and electronic structure difference of a single OV on the surfaces with different OV concentrations. (For interpretation of the references to colour in this figure legend, the reader is referred to the web version of this article.)

structure tuning, possibly because the relationship between the concentration of OVs and their structures remains unclear. Therefore, it is of great importance, but still a challenge to check whether the OV concentration change can realize the OV structure tuning.

In this study, taking BiOCl exposed with (001) surface as the example because of its OVs dependent photoreactivity and facile OVs generation ability under O_2 -deficient UV/thermal conditions or during photocatalysis [3,6,20–22], we first endeavor to clarify the relationship between the concentration of OVs and their structures, and thus develop an OV concentration mediated surface structure tuning method to improve the selectivity in photocatalytic oxidation of amines to imines under visible light. Herein the OV concentration change of BiOCl (001) surface is realized via a new H_2O_2 treatment coupled infrared irradiation method. Selective aerobic oxidation of a secondary amine N-tert-butylbenzylamine (BA) to N-tert-butylbenzylimine (BI) under visible light in acetonitrile solution is chosen as the model reaction (Eq. (1)), because this reaction proceeds without the assist of $\cdot OH$, which can avoid the fast mutual transformation of reactive oxygen species ($\cdot O_2^-$, H_2O_2 and $\cdot OH$) in aqueous solution [14,23,24], and thus favor our interpretation of OV concentration related photocatalysis mechanisms.



2. Experimental

2.1. Sample preparation

2.1.1. Synthesis of BiOCl nanoplate microspheres with OV (OV-3)

BiOCl nanoplate microspheres with OV on its {001} facet (OV-3) were synthesized using the solvothermal-induced hot ethylene glycol reduction. In a typical procedure, 3 mmol $\text{Bi}(\text{NO}_3)_3 \cdot 5\text{H}_2\text{O}$ and stoichiometric amounts of KCl were added into 16 mL ethylene glycol solution. The mixture was stirred for 0.5 h at room temperature, and then poured into a 20 mL Teflon-lined stainless autoclave. Subsequently, the autoclave was heated at 160 °C for 12 h, and then cooled down to room temperature. The resulting precipitates were collected and washed with deionized water and ethanol and dried at 60 °C in vacuum.

2.1.2. Synthesis of OV- x ($x = 0-2$)

A new H_2O_2 coupled infrared irradiation treatment was employed to synthesize OV-2 from OV-3. Typically, 0.5 g of OV-3 was mixed with H_2O_2 (1 mL, 10%) and dried under IR lamp in air, subsequently the dried powder was washed with deionized water and ethanol and dried at 60 °C in vacuum. The resulting samples were termed OV-2. OV-1 was obtained via OV-2 after the same H_2O_2 coupled infrared irradiation treatment. OV-0 was obtained by annealing OV-1 at 300 °C under O_2 atmosphere for 6 h to fully oxidize the surface.

2.1.3. Synthesis of BOC-001 and BOC-010

3 mmol of $\text{Bi}(\text{NO}_3)_3 \cdot 5\text{H}_2\text{O}$ and stoichiometric amounts of KCl were added in 30 mL distilled water with continuous stirring, and then KOH

was added to adjust the pH value of solution to 6.7. Subsequently, the solution was stirred for 30 min at room temperature and then poured into a 60 mL Teflon-lined stainless autoclave. Next, the autoclave was heated at 220 °C for 24 h, and then cooled down to room temperature. The resulting white precipitates were collected and washed with deionized water and ethanol and dried at 60 °C in air. The obtained white powder was (010) facet exposed BiOCl. In addition, the powder obtained without the addition of KOH under same condition was (001) facet exposed BiOCl. Then these BiOCl samples were dispersed in aqueous solution and subsequently irradiated by UV light for 1 h with Ar purging to craft surface OVs. The resulting light gray precipitates were collected and washed with ethanol and deionized water and dried at 60 °C in vacuum. The products obtained via (001) and (010) facet exposed BiOCl were denoted as BOC-001 and BOC-010, respectively.

2.2. Sample characterization

The powder X-ray diffraction (XRD) measurements were recorded on a Rigaku D/MAX-RB diffractometer with monochromatized Cu K α radiation ($\lambda = 0.15418$ nm). The scanning electron microscope (SEM) images were obtained with a SU8010 field-emission scanning electron microscope (Hitachi, Japan). Raman spectra were obtained by a confocal laser micro-Raman spectrometer (Thermo DXR Microscope, USA) with 532 nm or 780 nm laser. We experimentally found that 532 nm Raman and 780 nm Raman were sensitive to OVs characterization and OVs induced structure changes in BiOCl, respectively. So the 532 nm Raman was adopted to study the mechanism of OV- H_2O_2 interactions, while 780 nm Raman was used for the detection of OVs induced short-range lattice distortions. Electron paramagnetic resonance (EPR) spectra were recorded on a JEOL EMX EPR Spectrometer (Billerica, MA), TEMPO and Mn(II) were used as the standard sample and reference sample for the quantitative analysis, respectively. UV-vis absorption spectra of the samples were obtained using a UV-vis spectrophotometer (UV-2550, Shimadzu, Japan). The high-resolution transmission electron microscopy (HRTEM) images were performed on JEOL JEM-2010FEF. X-ray photoelectron spectroscopy (XPS) data were obtained using Perkin-Elmer PHI 5000C and all binding energies were corrected for specimen charging by referencing the C 1s peak to 284.8 eV. Bismuth L_{3-2} -edge extended X-ray absorption fine structure (EXAFS) spectra were performed at the beamline 1W1B of Beijing Synchrotron Radiation Facility, Institute of High Energy Physics, Chinese Academy of Sciences. O_2 temperature-programmed desorption experiments (O_2 -TPD) were recorded on AutoChem II 2920 (Micromeritics, USA) using a TCD detector. To analyze the evolved products in the gas phase, an on-line mass spectrometer was also used on several occasions. In a typical procedure, 0.1 g catalyst was pre-treated with pure He at 300 °C for 30 min, then cooled down to 80 °C in the same atmosphere and exposed to a mixture of O_2 and He at 80 °C for 1 h. Next, the catalyst was purged with pure He gas and the TPD measurement was carried out at a heating rate of 10 K min $^{-1}$ up to 500 °C. O_2 adsorption diffuse reflectance FTIR spectra (O_2 -FTIR) were recorded by Nicolet iS50 FTIR spectrometer (Thermo, USA). Samples were heated under vacuum (1×10^{-6} mbar) at 300 °C for 30 min, and

then cooled down to room temperature under vacuum. FTIR spectra of O₂ adsorption were obtained after O₂ (5 kPa) exposure at room temperature.

GC–MS measurements were made with a Thermo Trace 1300-ISQ equipped with a TG-5MS capillary column (5% phenyl methylpolysiloxane, 95% polydimethylsiloxane, 30 m, 0.25 mm × 0.25 μm, Thermo) using nitrogen as the carrier gas. Standard analysis conditions: injector temperature 250 °C, MS detector temperature: 280 °C, column temperature program: 80 °C (hold 3.6 min or 5.0 min) to 280 °C (hold 10.0 min). Flash column chromatography was performed using 200–300 mesh silica gel. ¹H NMR spectra were recorded on 400 MHz or 600 MHz spectrophotometers. Chemical shifts (δ) are reported in ppm from the solvent resonance as the internal standard (CDCl₃: 7.26 ppm). Data are reported as follows: chemical shift, multiplicity (s = singlet, d = doublet, t = triplet, dd = doublet of doublets, m = multiplet), coupling constants (Hz) and integration. ¹³C NMR spectra were recorded on 100 MHz with complete proton decoupling spectrophotometers (CDCl₃: 77.0 ppm).

2.3. DFT theoretical calculation

The theoretical calculations were performed using CASTEP package and VASP package. The generalized gradient approximation (GGA) with the Perdew-Burke-Ernzerhof (PBE) exchange-correlation function was employed [25]. The plane-wave pseudopotential approach and ultrasoft pseudopotentials were employed for all the atoms. During the geometrical optimization, all BiOCl configurations were fully relaxed with the P4/nmm symmetric constraints to an energy convergence of 10^{−5} eV/atom with a kinetic energy cutoff of 380 eV [26]. The Monkhorst-Pack mesh were 4 × 4 × 1 and 2 × 2 × 1 for the 2 × 2 and 4 × 4 surface, respectively. To simulate the O₂ adsorption/activation on BiOCl surfaces, models were performed with the exchange-correlation function described by GGA-PBE with a kinetic energy cutoff of 520 eV [27]. The energy converged to 10^{−5} eV/atom during the geometrical optimization. In the energy calculation, the k-points were increased to 6 × 6 × 2 and 3 × 3 × 2 for the 2 × 2 and 4 × 4 surface, respectively. The vacuum in all models was kept at 12 Å.

2.4. Electrochemical measurements

Electrochemical properties of BiOCl were investigated on a CHI electrochemical workstation (660B, Shanghai, China) with the BiOCl electrode as the working electrode, a Pt plate as the counter electrode and a saturated calomel electrode (SCE) as a reference electrode. BiOCl electrode was prepared as follows: 5 mg BiOCl (OV-0) was ultrasonically dispersed in 0.5 mL Nafion solution (2 wt.% in isopropanol) and then dip-coated the slurry onto a FTO glass electrode (1 × 3 cm). The Mott-Schottky curve of OV-0 was measured at a frequency of 100 Hz in a 40 mL of 0.1 M NaClO₄ acetonitrile solution.

To investigate the oxidation potential of BA and BI, cyclic voltammograms of BA and BI were measured in a 40 mL 0.1 M NaClO₄ acetonitrile solution to obtain the onset potentials of BA and BI oxidation, with the carbon glass electrode as working electrode, a Pt plate as the counter electrode and a saturated calomel electrode (SCE) as a reference electrode. The onset potentials of BA and BI oxidation were estimated to be 1.21 V and 2.02 V (NHE), respectively (Fig. S1a).

2.5. Determination of the band edge positions of OV-x (x = 0–3)

Theoretical prediction of conduction band (CB) and valence band (VB) for BiOCl were calculated by Eqs. (2) and (3) as follows [28].

$$E_{CB} = X - E^{\circ} - 1/2E_g \quad (2)$$

$$E_{VB} = E_{CB} + E_g \quad (3)$$

where X is the Mulliken electronegativity of the BiOCl, E[°] is the scale

factor relating the reference electrode redox level to the absolute vacuum scale (4.60 eV for acetonitrile solution), and E_g is the bandgap of the BiOCl. The calculated CB and VB of BiOCl were 0.09 and 3.44 eV, respectively. This was close to the result of Mott-Schottky plots on OV-0 (CB = 0.15 V vs. NHE, Fig. S1b). Bandgap energies of OV-0, OV-1, OV-2 and OV-3 were estimated to be 3.35, 3.23, 3.14 and 3.00 eV, respectively, which were calculated from the Tauc plots (Fig. S1c). Relative VB positions of OV-x (x = 0–3) were determined by valence band XPS spectra (Fig. S1d). The VB positions of OV-1, OV-2, and OV-3 shifted towards CB by 0.07, 0.11 and 0.21 eV, respectively, in comparison with that of OV-0.

2.6. Photocatalytic aerobic amine oxidation

In a typical reaction, 0.05 mmol BA and 60 mg photocatalyst were added to 5 mL acetonitrile in a 10 mL round-bottom flask with continuous stirring. The flask was sealed with a rubber stopper wrapped in aluminum foil, connected to air through a syringe needle, immersed in cool water between 21 and 25 °C, and irradiated by a 300 W Xenon lamp (cutoff light below 420 nm when simulating the visible light) from the side face. The reaction conversion and selectivity were determined by an internal standard curve method with GC–MS using 1,4-diisopropylbenzene as internal standard [22].

2.7. Electrocatalytic aerobic amine oxidation

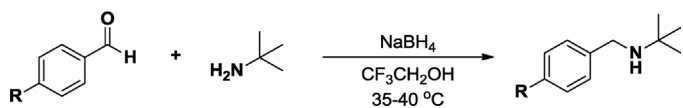
Electrocatalytic aerobic oxidation of BA to BI was conducted in a conventional H-type glass cell separated by a proton exchange membrane in between. 0.3 mmol BA, 30 μL 30% H₂O₂ solution and 0.45 g 3 Å sieves were added into the same compartment with continuous stirring, with carbon glass electrode as working electrode (operating voltage: +2.15 V vs. NHE), a Pt plate as the counter electrode, a saturated calomel electrode (SCE) as a reference electrode and 60 mL 0.1 M NaClO₄ acetonitrile solution as the supporting electrolyte.

2.8. Determination of H₂O₂ concentration

0.5 mL acetonitrile solution obtained after the photocatalytic aerobic amine oxidation was diluted in water to form a 4 mL solution, then a (p-hydroxyphenyl) acetic acid (POHPAA) method was used [29]. The reaction product of H₂O₂ with POHPAA fluorescence reagent had a strong fluorescent emission at 409 nm when excited at 315 nm.

2.9. Preparation of the para-substituted BA substrates

General procedure for the preparation of substrates (R = MeO, Me, H, Cl, and CF₃) [30].



A solution of the aldehyde (1 mmol) and TFE (2 mL) was magnetically stirred at 35–40 °C. After 5 min, 2-methylpropan-2-amine (1 mmol) was added, and the mixture was vigorously stirred. After stirring for 5 min, NaBH₄ (1.2 mmol) was added. After completion of the reaction (monitored by TLC), the mixture was filtered and the residue was washed with TFE (2 mL). The solvent was concentrated and purified by flash column chromatography, eluting with petroleum ether and ethyl acetate to afford the corresponding products.

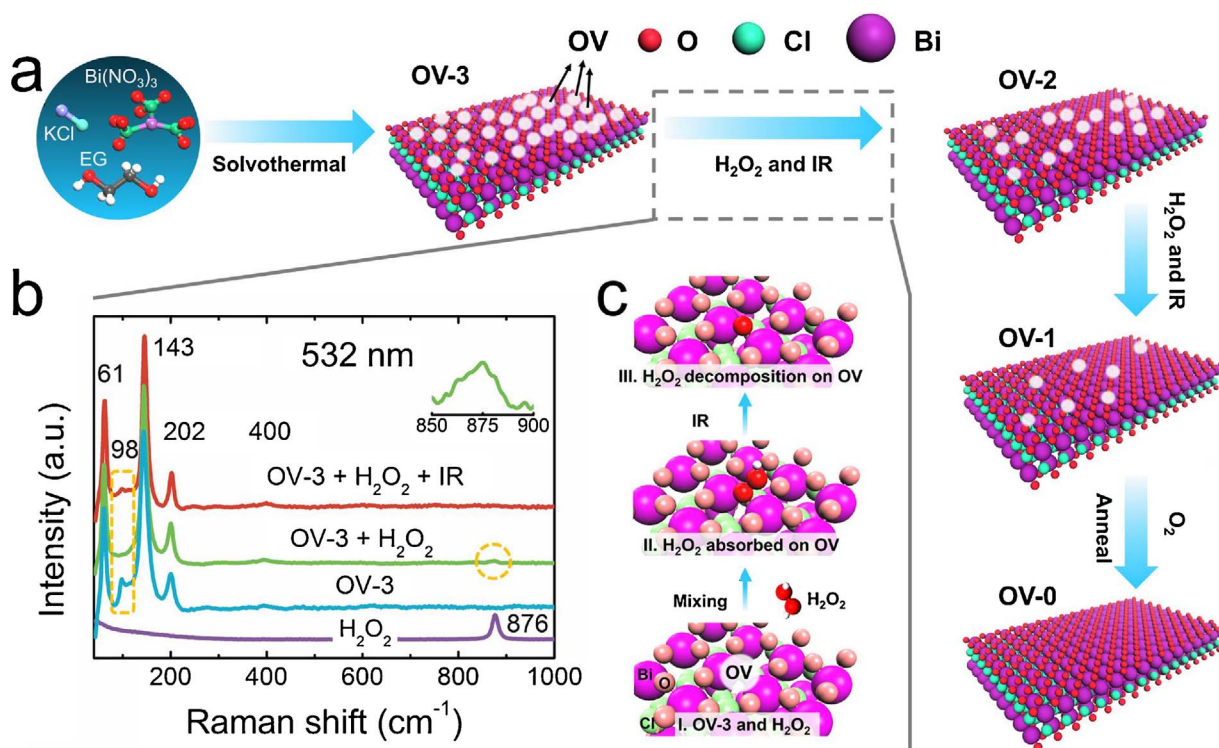


Fig. 2. (a) The synthesis process of BiOCl samples with different OV concentration. (b) *In-situ* Raman spectra of OV-3 treated with H_2O_2 and infrared irradiation. (c) The H_2O_2 dissociative adsorption and *in-situ* decomposition on the OV of BiOCl.

3. Results and discussion

3.1. Catalyst preparation and characterization

The BiOCl samples of different OV concentrations were produced by solvothermal-induced hot ethylene glycol reduction, followed with a new H_2O_2 treatment coupled infrared irradiation method for the OV concentration tuning (Fig. 2a). Three resulting BiOCl samples exposed with (001) surface were denoted as OV-1, OV-2 and OV-3, which possessed the lowest, medium, and highest OV concentrations, respectively. A control sample without OV (OV-0) was then prepared by annealing OV-1 at 300°C under O_2 atmosphere. Because the oxygen vacancies of OV-1 could not be thoroughly quenched even after six cycles of H_2O_2 oxidation coupled IR irradiation treatment, we thus employed the annealing under O_2 atmosphere to completely remove oxygen vacancies (Fig. S2). The OV concentration tuning mechanism of this new H_2O_2 treatment coupled infrared irradiation method was revealed by the *in-situ* Raman spectroscopy. OV-3 demonstrated typical four BiOCl Raman active modes with frequencies at 61, 143, 202, and 400 cm^{-1} and an additional peak at 98 cm^{-1} corresponding to OV [21,31]. After OV-3 was treated with H_2O_2 , the peak at 98 cm^{-1} corresponding to OV disappeared, accompanying with the appearance of a new anisotropy peak at 875 cm^{-1} which was assigned to O–O bond in adsorbed H_2O_2 , because this peak was close to that of pure H_2O_2 centered at 876 cm^{-1} (Fig. 2b). This result indicated that H_2O_2 was chemisorbed on the OVs of BiOCl and then received electrons from OVs, which was further confirmed by the density functional theory (DFT) calculation results (Fig. S3), accompanying with the disappearing of the OV peak at 98 cm^{-1} and the O–O (in H_2O_2) peak shift to lower wavelength. After the infrared irradiation, the Raman peak at 875 cm^{-1} disappeared and the peak at 98 cm^{-1} re-emerged but with decreased intensity, indicating the partial quenching of OV on OV-3 after H_2O_2 treatment and infrared irradiation. The H_2O_2 dissociative adsorption and *in-situ* decomposition process was schematically illustrated in Fig. 2c.

All the four BiOCl samples (OV-0, OV-1, OV-2 and OV-3) shared the same tetragonal structure with a space group of $P4/nmm$ and a $D74h$ symmetry according to X-ray diffraction (XRD) patterns analysis, and consisted of nanoplate microspheres of diameter from 0.5 to $2\text{ }\mu\text{m}$ (Fig. S4). Their nanoplates were exposed with {001} facets according to the analysis of scanning electron microscope (SEM) and high-resolution transmission electron microscopic (HRTEM) images (Fig. S5). Obviously, the OV concentration change *via* the H_2O_2 treatment coupled infrared irradiation method did not affect the phase and morphology of BiOCl.

As the generation of OVs was quantitatively accompanied with the appearance of $\text{Bi}^{(3-x)+}$ [20], we first estimated the OV concentrations of four model BiOCl samples via measuring the $\text{Bi}^{(3-x)+}$ content by X-ray photoelectron spectroscopy (XPS) analysis (Fig. S6). The $\text{Bi}^{(3-x)+}$ contents of OV-0, OV-1, OV-2 and OV-3 were calculated to be 0, 10%, 15% and 19%, respectively, confirming their increased OV concentrations. Subsequently, their OV concentrations were further estimated by the double integration of OV peaks at $g = 2.002$ in their electron paramagnetic resonance (EPR) spectra, which were 0, 0.026%, 0.037% and 0.052% for OV-0, OV-1, OV-2 and OV-3 according to the OV/ e^- model (a OV contains one excess electron) [32]. For the EPR measurements, 2,2,6,6-tetramethylpiperidinyloxy (TEMPO) and Mn(II) were used as the standard sample and reference sample, respectively (Fig. 3a,b). Given that XPS is sensitive to the surface chemical environment of the material, while EPR gives the information of unpaired electrons on both surface and bulk of the material, this difference of OV concentration between XPS methods (high surface OV concentration) and EPR methods (low overall OV concentration) indicated that the OVs were mainly on the surface of those BiOCl samples.

3.2. The relationship between OV concentration and OV structure

The relationship between OV concentration and its structure of BiOCl was studied by experimental characterizations and first principle calculations. The OV concentration change was supposed to alter the

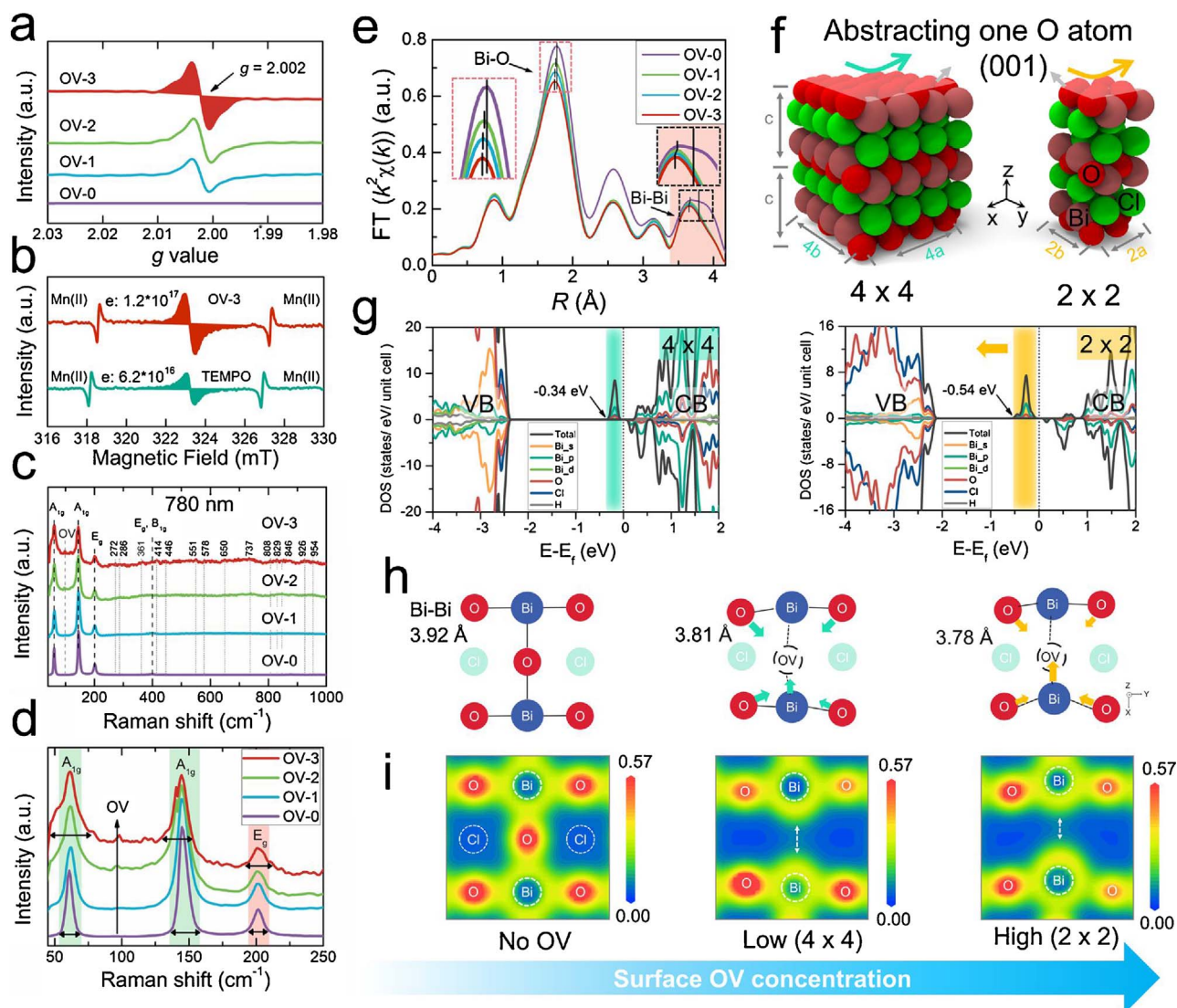


Fig. 3. (a) EPR spectra of OV- x ($x = 0-3$) with the same weight (red area showed the integration method for OV quantification). (b) Quantification of the OV concentration of OV-3 using TEMPO and Mn(II), the amount of unpaired electrons in 0.1 g OV-3 is estimated to be 1.2×10^{17} . (c, d) 780 nm Raman spectra (the number of forbidden modes are 0, 1, 5, 12 for OV-0, OV-1, OV-2 and OV-3, respectively). (e) Fourier-transform Bi L_3 -edge EXAFS spectra of OV- x ($x = 1, 2$ and 3). (f) Schematic illustration of the atomic structure of low (4×4) and high (2×2) OV concentration model, respectively. (g) Calculated DOS of BiOCl with low (left) and high (right) OV concentration on the (001) facet, the labeled peaks blew CB are OV states. (h) OV structures (OV surrounding 8 atoms; arrows indicate the atoms movement in the xy plane), and (i) corresponding electron density maps of BiOCl with different OV concentration. (For interpretation of the references to colour in this figure legend, the reader is referred to the web version of this article.)

distortion of OV surrounding atoms, as confirmed by the following structural characterizations of these BiOCl samples of different OV concentrations. First, HRTEM images revealed that disordered structures were covered on the surface of crystalline BiOCl samples with OVs, and the thickness of disordered shell increased along with improving the OV concentration. On the contrary, similar disordered structures did not appear on the surface of BiOCl without OVs (Fig. S5). Obviously, these disordered structures were arisen from the atom distortions associated with OVs. Raman spectra, being sensitive to the short-range lattice distortion, were then used to examine the structural difference of these BiOCl samples (Fig. 3c,d). Besides the typical four BiOCl Raman active modes with frequencies at 61, 143, 202 and 400 cm^{-1} in the Raman spectra of BiOCl, the formation of OVs induced a new peak at 98 cm^{-1} corresponding to OVs, and the intensity of this new peak increased from OV-0 to OV-3. Meanwhile, the Bi-Cl peaks ($2A_{1g}$ and E_g) broadened and the forbidden active modes increased along with increasing the OV concentration. These peak broadening and forbidden active mode increasing were originated from the typical phonon confinement effects induced by atom distortions [33,34],

indicative of the short range structural difference between the four samples. Both HRTEM images and Raman spectra suggested that the surface structures of BiOCl were strongly associated with its OV concentration even without changing facet exposure, which was further unraveled by extended X-ray absorption fine structure (EXAFS) spectroscopy. In the Fourier transform spectra of the Bi L_3 -edge EXAFS oscillations (Fig. 3e), two sharp peaks around 1.8 \AA and 3.7 \AA were assigned to Bi-O and Bi-Bi, respectively. The formation of OVs decreased Bi-O peak intensities of OV-1, OV-2 and OV-3 because of less O atoms coordinated with Bi atoms. Meanwhile, the lengths of Bi-O and Bi-Bi were shortened by $0.02-0.03 \text{ \AA}$ and $0.13-0.15 \text{ \AA}$, respectively. The bond length shortening was attributed to the surrounding atoms distortion induced by the OV formation. Moreover, the intensity of Bi-O peak was further decreased and the lengths of Bi-O and Bi-Bi were further shortened along with the OV concentration increase.

To further investigate the electronic structure of BiOCl with different OV concentration on its {001} facet, we constructed two atomic models with different OV concentration according to the EXAFS results, of which higher OV concentration surface possessed shorter Bi-O/

Bi–Bi lengths (Fig. 3f). Subsequently, we employed first-principles DFT to calculate the atomic structure associated electronic structure (density of states; DOS) [35]. DFT calculation results revealed that the OV states were mainly came from the 6p orbitals of Bi atoms and tailed towards valence band (VB) about 0.2 eV along with increasing the OV concentration, resulting in reduced band gap and promoted light adsorption for BiOCl in case of higher OV concentration, which was consistent with their UV–vis diffuse reflectance spectra (DRS) results (Fig. 3g and S7). Moreover, the electron density of OV was mainly localized at the center of OV surrounding Bi atoms for low OV concentration surface, but partially departed from Bi atoms to the position of abstracted oxygen atom on the high OV concentration surface. This meant more electrons on OVs became less localized at higher OV concentration, as the bond lengths of Bi–Bi and Bi–O near OV were shortened (Fig. 3h and i). On the basis of above experimental and theoretic results, we could summarize the OV concentration-structure relationship as higher OV concentration would result in the bond length shortening of Bi–Bi and Bi–O near OV and more electrons on OVs being less localized.

3.3. OV concentration associated O_2 adsorption/activation

To check whether such an OV concentration-structure relationship could affect O_2 adsorption/activation and thus modulate the active species generation for the desired reactions, we subsequently investigated O_2 adsorption/activation on the four BiOCl samples with temperature-programmed desorption (TPD), diffuse reflectance Fourier transform infrared (FTIR) spectroscopy and DFT calculations. In the O_2 -TPD spectra (Fig. 4a), the desorption peak of O_2 around 300 °C, which is related to chemisorbed O_2 , appeared on the three samples bearing OVs, but was not observed on OV-0 without OVs. This difference indicated that OVs were active centers for the O_2 adsorption/activation. Along with increasing the OV concentration, the areas of O_2 desorption peaks improved accordingly, further confirming the function of OVs as active centers and the dependence of O_2 adsorption on the amount of OVs. More interestingly, all the desorption peaks were of the anisotropic characteristic and could be divided into two parts, which were labeled as red and blue in Fig. 4a. The ratios of red part to blue part ascended with increasing the OV concentration, which were 0.3, 0.5 and 1.7 for OV-1, OV-2, and OV-3 respectively. These two parts might be arisen

from different adsorbed oxygen species such as adsorbed O_2^- or O_2^{2-} , which could not be distinguished by TPD analysis. Therefore, we utilized the FTIR technique to further differentiate them (Fig. 4b). For the $^{16}O_2$ adsorption, two bands around 885 and 1120 cm^{-1} , being assigned to adsorbed $^{16}O_2^{2-}$ and $^{16}O_2^-$ respectively [36], were observed for the three samples bearing OV, confirming that O_2 could be reduced to both O_2^- and O_2^{2-} on the OVs of BiOCl. Subsequently, the $^{18}O_2$ adsorption was conducted on OV-3 of highest oxygen vacancy concentration. These two bands appeared around 840 and 1066 cm^{-1} in the case of $^{18}O_2$. The experimental ratio of $\nu^{16}O_2/\nu^{18}O_2$ (1.05; 1120 $cm^{-1}/1066$ cm^{-1}) was very close to the theoretical isotope ratio of 1.06 ($(18/16)^{1/2}$), confirming the assignments of these two bands around 885 and 1120 cm^{-1} to adsorbed O_2^{2-} and O_2^- . As shown in Fig. 4b, BiOCl with higher OV concentration possessed higher ratio of O_2^{2-}/O_2^- , so the red part in TPD spectra could be arisen from the O_2^{2-} adsorption, and the blue part represented the O_2^- adsorption. We therefore concluded that both O_2^{2-} and O_2^- were adsorbed on the OV of BiOCl, and the BiOCl (001) surface of higher OV concentration favored the O_2^{2-} adsorption.

To further demystify this OV concentration associated molecular oxygen adsorption/activation behavior, we theoretically simulated the adsorption/activation process on the BiOCl (001) surface. When molecular oxygen was adsorbed on 4×4 (low OV concentration) and 2×2 (high OV concentration) surfaces, the most favorable adsorption mode was end-on O_2^- via a one-electron transfer on both surfaces with the O–O bond length (~ 1.34 Å) close to that of $\cdot O_2^-$ (1.26 Å), consistent with our previous result [3]. Interestingly, the adsorption of side-on O_2^{2-} via a two-electron transfer was also observed as metastable state on both surfaces, with the O–O bond length (~ 1.40 Å) close to that of O_2^{2-} (1.49 Å) (Fig. 4c and S8). The energy difference of approximately 0.6 eV between O_2^- adsorption and O_2^{2-} adsorption on the 2×2 surface was smaller than that (0.8 eV) on the 4×4 surface (Fig. 4d), indicating that the O_2^{2-} adsorption was more kinetically favorable on the BiOCl (001) surface of higher OV concentration, in good agreement with the above experimental results. Therefore, both experimental and theoretic results confirmed that increasing OV concentration could shift the O_2 chemisorption states on OVs of BiOCl to further modulate the generation of active species during photocatalysis.

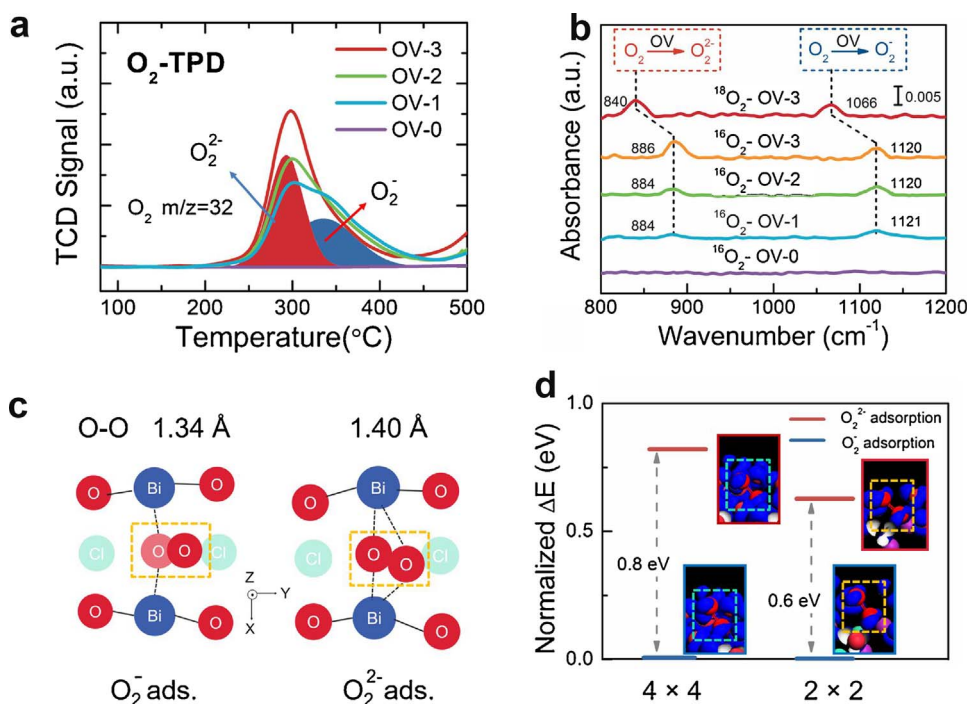


Fig. 4. (a) O_2 -TPD (two labeled parts were derived from the anisotropy peak of OV-3), and (b) O_2 -FTIR of OV-x ($x = 0-3$). (c) DFT calculation results of end-on O_2^- adsorption (left; with the O–O distance of 1.34 Å) and side-on O_2^{2-} adsorption (right; with the O–O distance of 1.40 Å) on high OV concentration surface (4×4 surface). (d) Normalized energy gap between side-on O_2^{2-} and end-on O_2^- adsorption on 4×4 surface (low OV concentration) and 2×2 surface (high OV concentration) surface, respectively. Inset: the corresponding charge concentration difference of different oxygen activation configurations showing varied electron density on the end O atom of the adsorbed O_2 .

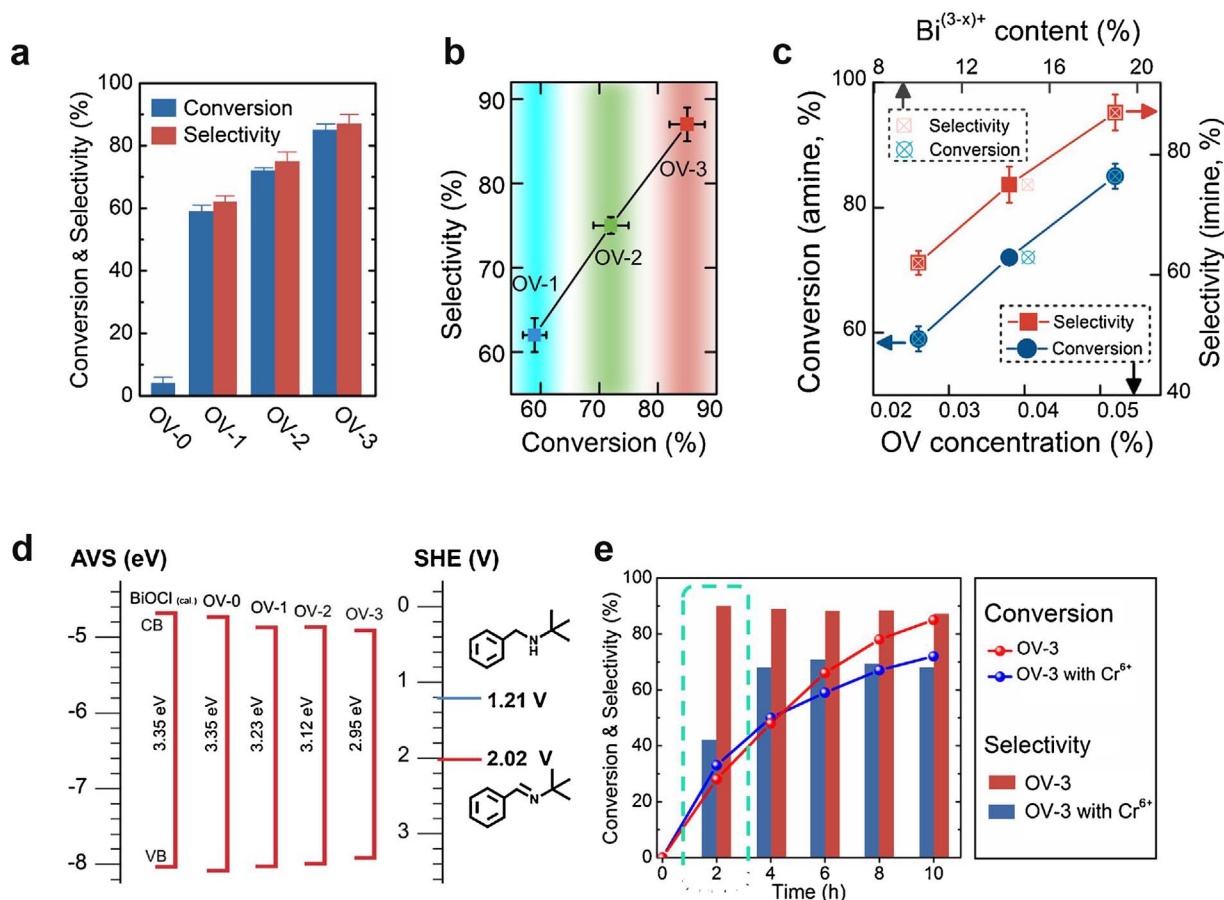


Fig. 5. (a) Photocatalytic aerobic oxidation of BA to BI on OV-*x* (*x* = 0–3) under visible light. Reaction conditions: catalyst (60 mg), BA (0.05 mmol), CH₃CN (5 mL), O₂ pressure (1 atm), 10 h, Xe lamp (> 420 nm) irradiation. (b) The relationship between conversion and selectivity of OV-*x* (*x* = 1–3). (c) The positive correlation between OV concentration and photocatalytic selective oxidation performance. (d) Band edge positions of OV-*x* (*x* = 0–3) relative to the oxidation potential of BA and BI in acetonitrile, BiOCl_(cal.) represented the result calculated with Mulliken electronegativity, which was in good agreement with the experimental one (OV-0). (e) Role of oxygen activation in amines oxidation on OV-3. Additional reaction conditions: Cr⁶⁺ (6.7 μmol, 0.08 mL), 3 Å sieves (0.5 g, when 3 Å sieves were added to absorb water, the conversion and selectivity were both slightly increased on OV-3). The reaction conversion and selectivity shown in (a–c and e) represented the average values of three independent experiments. The standard deviations of both conversion and selectivity in (e) were within 6%, and the error bars were not labeled for the sake of presentation.

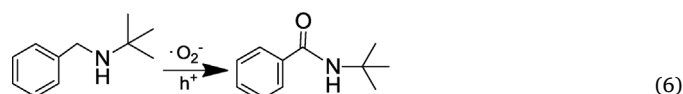
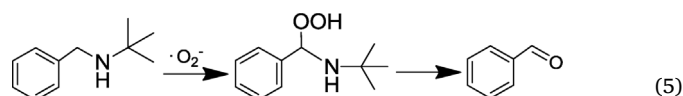
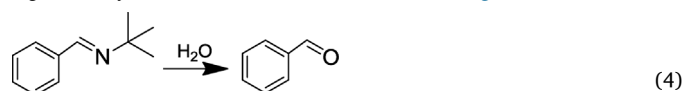
3.4. Photocatalytic aerobic amine oxidation

Under visible light, the overall BA conversions of OV-0, OV-1, OV-2, and OV-3 were 4%, 59%, 72% and 85%, with corresponding BI selectivity of 0, 62%, 75% and 87%, respectively (Fig. 5a and Table S1). These results demonstrated an interesting positive correlation between OV concentration and photocatalytic selective oxidation performance (Fig. 5b and c). The contributions of different surface area and BA adsorption ability were ruled out, as the four samples had similar BET surface areas and BA adsorption capacities (Table S2). Meanwhile, residual H₂O₂ was not detected on the three samples with oxygen vacancy after the H₂O₂ treatment coupled infrared irradiation process according to the results of Raman spectra and O 1s XPS spectra (Fig. 3b and S9). Although we could easily attributed the enhanced BA conversion of OV-1, OV-2, and OV-3 to their increased visible light absorbance arising from higher OV concentration (Fig. S7), their increased visible light absorbance was not able to account for the interesting OV concentration associated BI selectivity in this study.

3.5. Mechanism study of OV concentration associated BI selectivity

It is known that high selectivity of photocatalysts depends on the generation of oxidants to activate reactants, but not to oxidize the products in a typical selective oxidation reaction [23,37–39]. In this study, both h⁺ generated on the VB of BiOCl and ROS (·O₂[−] and O₂^{2−}) may participate in the photocatalytic aerobic BA oxidation. As these

four OV-*x* (*x* = 0–3) samples almost shared the same VB positions, and their photogenerated h⁺ could oxidize both the reactant and the product (Fig. 5d and S1), which was not the key factor to achieve the high selectivity in this reaction, so the high selectivity in the oxidation of amines to imines could not be explained by the conventional VB position dominated selective oxidation [23,38], but a novel ROS associated mechanism. This novel mechanism was confirmed by the O₂ control experiment as follows. When replacing the air or O₂ atmosphere with Ar, the BI selectivity decreased (Table S3). Also, when Cr⁶⁺ was added as a competitive electron acceptor for O₂, the BI selectivity decreased significantly from 90% to 42% in the first 2 h (Fig. 5e).



To clarify the ROS dependent selective BA oxidation of BiOCl with OVs under visible light, we thus investigated the photocatalytic ROS (·O₂[−] and O₂^{2−}) generation over OV-*x* (*x* = 0–3). ·OH was neglected in this study because of its negligible amount, which was not detected by

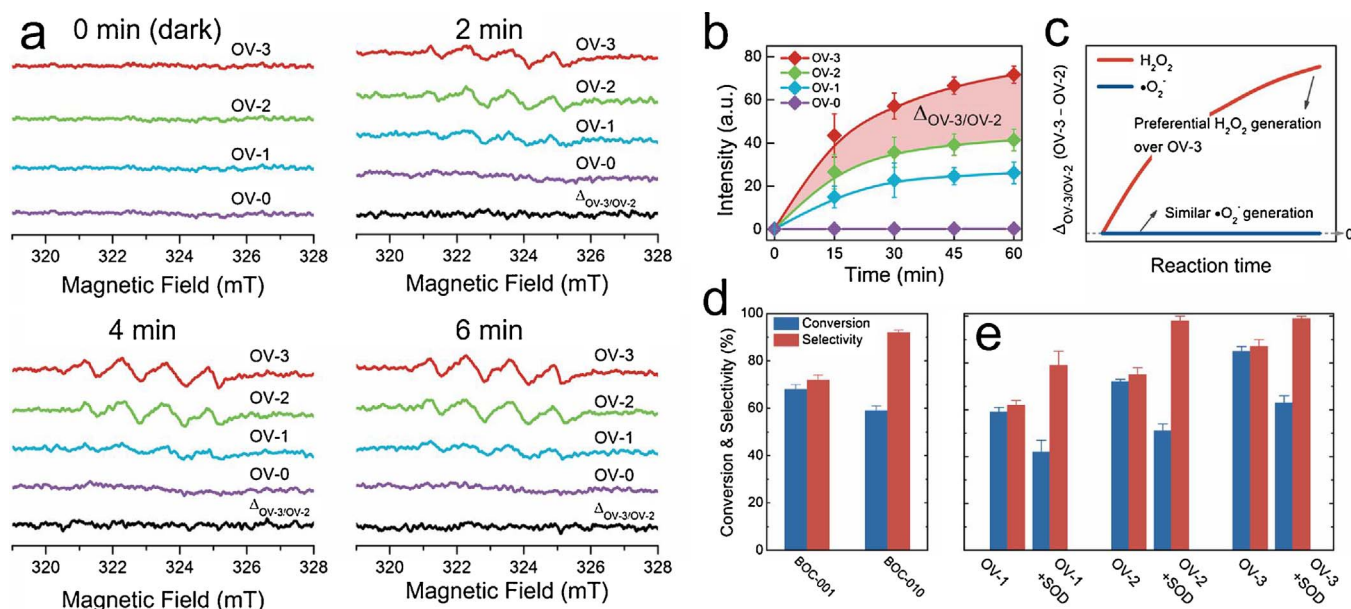


Fig. 6. (a) Time dependence of generated $\cdot\text{O}_2^-$ radical and corresponding differential spectrum over OV- x ($x = 0-3$) under visible light irradiation, recorded by *in-situ* EPR spectra using 5, 5-dimethyl-1-pyrroline-N-oxide (DMPO) as a spin trapper. $\Delta_{\text{OV-3/OV-2}}$ was the difference spectrum between OV-3 and OV-2 (OV-3 – OV-2). (b) Time dependence of H_2O_2 concentration over OV- x ($x = 0-3$). (c) ROS difference between OV-3 and OV-2. OV-3 and OV-2 differed in the H_2O_2 generation while generated similar amount of $\cdot\text{O}_2^-$, indicating that OV-3 possessed higher ratio of $\text{H}_2\text{O}_2/\cdot\text{O}_2^-$ than OV-2 during photocatalysis. Photocatalytic performance of BOC-010/BOC-001 (d) and OV- x ($x = 1-3$) (e) for the aerobic oxidation of BA.

the *in-situ* EPR measurements (Fig. 6a), although the sensitivity of EPR could reach about 10^{12} spins (*ca.* 10^{-12} moles) at room temperature [40]. Although more $\cdot\text{O}_2^-$ was generated over OV-2 and OV-3 than OV-1, the generation of $\cdot\text{O}_2^-$ over OV-2 was almost the same as that over OV-3 (Fig. 6a), ruling out the contribution of $\cdot\text{O}_2^-$ generation to their different BI selectivity of OV-2 and OV-3. Interestingly, the amounts of H_2O_2 generated over the four samples were positively correlated to their OV concentration, while OV-3 could generate more H_2O_2 than OV-2 (Fig. 6b). Therefore, we assumed that highly selective photocatalytic BA oxidation mechanism of BiOCl was determined by the favorable generation of H_2O_2 (O_2^{2-}) over BiOCl with high OV concentration (Fig. 6c). To confirm this assumption, two BiOCl samples exposed with (001) or (010) surface (denoted as BOC-001 and BOC-010) were used for photocatalytic BA oxidation, as BOC-001 preferred to generate $\cdot\text{O}_2^-$, while BOC-010 favored the formation of O_2^{2-} according to our previous report [3,15]. Under visible light, BOC-010 exhibited higher selectivity than BOC-001 on the selective oxidation of BA to BI (92% for BOC-010 and 72% for BOC-001) (Fig. 6d), strongly validating that H_2O_2 (or O_2^{2-}) was beneficial for the selectivity of BA oxidation.

Subsequently, we carried out ROS trapping experiments to check the role of $\cdot\text{O}_2^-$ on the selective oxidation of BA to BI (Fig. 6e), and found that the addition of superoxide dismutase (SOD, which could catalyze the disproportionation of $\cdot\text{O}_2^-$ into O_2 and H_2O_2) significantly increased the BI selectivity from 62% to 79% for OV-1, from 75% to 98% for OV-2, and from 87% to 99% for OV-3, respectively. These results confirmed that H_2O_2 (O_2^{2-}), instead of $\cdot\text{O}_2^-$, accounted for the high BI selectivity during the photocatalytic BA oxidation over BiOCl. To further figure out the role of $\cdot\text{O}_2^-$ during BA oxidation, we analyzed the byproducts of photocatalytic BA oxidation with using gas chromatography-mass spectrometry (GC-MS), and found that benzaldehyde was a major component, accompanying with minor *N*-(tert-butyl)benzamide (Fig. S10). It is known that benzaldehyde may derive from the hydrolysis of BI with *in-situ* generated H_2O (Eq. (4)) and/or over oxidation by $\cdot\text{O}_2^-$ (Eq. (5)), while *N*-(tert-butyl)benzamide can be produced by the $\cdot\text{O}_2^-$ nucleophilic attack via Eq. (6) [39,41–43], further confirming that $\cdot\text{O}_2^-$ did not contribute to the selective oxidation of BA. Therefore, the above experimental and theoretical results pointed out that the favorable molecular oxygen activation to O_2^{2-} at high OV

concentration strongly accounted for OV concentration associated BI selectivity of BiOCl with OVs on the aerobic BA oxidation under visible light.

On the basis of the above results and discussion, we proposed a possible mechanism to explain the visible light driven selective aerobic BA oxidation on the BiOCl (001) surface as follows. First, charge carriers (h^+/e^-) were generated in BiOCl with OVs under visible light irradiation. BA was then oxidized by h^+ to generate corresponding aminium cation radical, accompanying with the molecular oxygen activation by e^- to produce ROS on OVs. Finally, the *in-situ* generated aminium cation radical reacted with ROS to form the BI product. During the oxygen activation process, BiOCl (001) surface of low OV concentration favored the formation of $\cdot\text{O}_2^-$ via a one-electron reduction pathway (Fig. 7a), but the counterpart of high OV concentration surface preferred to activate molecular oxygen to generate O_2^{2-} via a two-electron reduction pathway (Fig. 7b), because Bi–Bi and Bi–O bond lengths were shortened and more electrons were less localized on the BiOCl (001) surface of high OV concentration. As the selectivity of BI is highly dependent on the generation of O_2^{2-} and/or H_2O_2 , BOC-001 of higher OV concentration exhibited much higher BI selectivity than its counterpart of lower OV concentration. To confirm this proposed mechanism, we first checked the generation of key intermediate aminium cation radical by the Hammett plot method and EPR spectra. The oxidation rates of *para*-substituted BA (MeO, Me, H, Cl, and CF_3 groups, Supporting Information) were examined to obtain the Hammett plot [44]. A satisfactory linearity ($\rho = -0.15$, $R^2 = 0.95$) was obtained between the $\log(k_x/k_H)$ values and the σ^+ constants (Fig. 8a), indicative of the carbocationic intermediates generation. Subsequently, the EPR spectra was further employed to check the generation of these intermediates. A six-line EPR signal on the OV-3-BA mixture emerged after visible light irradiation (Fig. 8b). Given that pure BA or OV-3 under visible light irradiation did not produce such a signal, the formation of this radical can be attributed to the photocatalytic BA oxidation, which can be induced either by ROS ($\cdot\text{O}_2^-$ and O_2^{2-}) or h^+ . In this study, h^+ was thought to be responsible for this radical generation, as this EPR signal was only slightly suppressed when O_2 atmosphere was replaced with Ar. Therefore, this EPR signal can be assigned to the nitrogen-centered or carbon-centered radical, which could be transformed mutually [45], confirming the generation of aminium

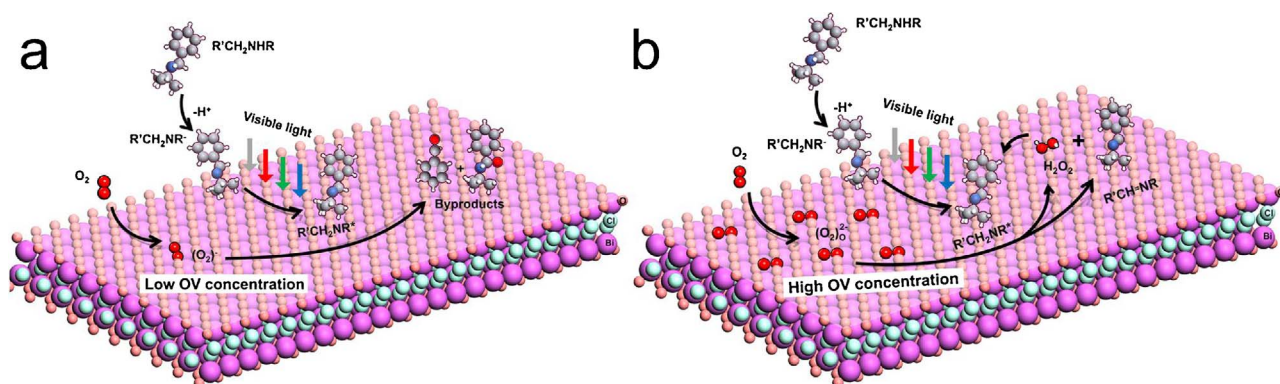


Fig. 7. Reaction scheme for the aerobic oxidation of BA to BI on BiOCl {001} facets with low (a) or high (b) OV concentration under visible light. R = *t*-Bu, R' = Ph. Only the most favorable reaction pathways on each surfaces were presented while others (such as small proportion of two-electron-transfer oxygen activation on low OV concentration surface or one-electron-transfer oxygen activation on high OV concentration surface) were neglected for the sake of presentation.

cation radical. Finally, we verified the reaction between aminium cation radical and H_2O_2 (O_2^{2-}) by electrocatalytic oxidation of BA to BI (Fig. 8c). During the electrocatalytic oxidation of BA, the aminium cation radical was generated by the anodic oxidation of BA [46], and then further oxidized to BI. Such an electrocatalytic oxidation of BA to BI proceeded at a very low selectivity (7%) without H_2O_2 . As expected, the addition of H_2O_2 largely increased the BI selectivity from 7% to 25% in the case of electrocatalytic BA oxidation. Because H_2O_2 could not oxidize BA directly (Table S1), this selectivity increase solidly supported that H_2O_2 could react with aminium cation radical to significantly enhance the BI selectivity.

3.6. The generality of OV concentration associated selectivity enhancement

We checked the generality of this OV concentration associated selectivity enhancement with (010) facet exposed BiOCl. The reaction selectivity increased with the OV concentration (Table S4, Supporting Information), which was similar to the case of (001) exposed BiOCl samples, suggesting this OV concentration modulated selectivity mechanism could be extended to BiOCl with different facet exposure. We also testified the applicability of such a mechanism on typical oxides such as TiO_2 (P25) and Nb_2O_5 . OVs on these two photocatalysts were generated via a typical vacuum coupled UV method [18,19,47,48]. By controlling the reaction time of vacuum treatment and UV irradiation, TiO_2 and Nb_2O_5 samples of different OV concentrations were obtained for photocatalytic BA oxidation. A similar positive correlation between OV concentration and selectivity was observed (Table S5). These results indicated the generality of this OV concentration modulated selectivity mechanism.

4. Conclusions

In summary, we have demonstrated the oxygen vacancy concentration associated selectivity improvement in aerobic photocatalytic amines to imines on BiOCl under visible light. Theoretical and experimental results revealed that the OV concentration increase could shorten the lengths of OV vicinal Bi–Bi and Bi–O bonds and also enrich electrons being less localized. These oxygen vacancy concentration associated BiOCl (001) surface structure changes favored the “side-on” molecular oxygen adsorption on the two OV vicinal Bi atoms, and thus shifted the molecular oxygen activation process from a one-electron reduction to a two-electron transfer, resulting in the formation of O_2^{2-} (H_2O_2) to realize higher selectivity in photocatalytic oxidation of benzylamines to benzylimines. This OV concentration mediated structure tuning method could also be used to increase the selectivity of other photocatalysts (TiO_2 and Nb_2O_5) in photocatalytic oxidation of amines to imines, suggesting its generality for the OV structure tuning. These findings deepen our understanding of OV associated structure change during photocatalysis, and also shed light on designing high-performance photocatalysts for selective oxidation of amines, especially for their band edge positions cannot match the redox potentials of a desired reaction.

Acknowledgment

This work was supported by National Natural Science Funds for Distinguished Young Scholars (Grant 21425728), National Key Research and Development Program of China (Grant 2016YFA0203002), National Science Foundation of China (Grant 51472100), Self-Determined Research Funds of CCNU from the

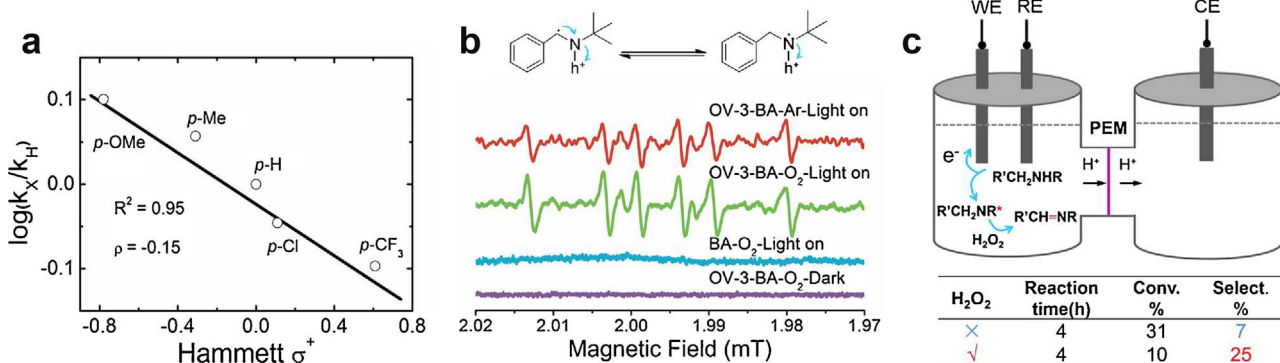


Fig. 8. (a) Hammett plots for the oxidation of *para*-substituted BA on OV-3. R = *t*-Bu, R' = Ph. (b) EPR detection of carbon-centered or nitrogen-centered radicals under different reaction conditions. (c) Electrocatalytic aerobic oxidation of BA to BI in an H-cell separated by a proton exchange membrane (PEM).

Colleges' Basic Research and Operation of MOE (Grant CCNU14Z01001), and Graduate Education Innovation Funding Project Grant from CCNU (2016CXZZ54). We also thank the National Supercomputer Center in Jinan for providing high performance computation.

Appendix A. Supplementary data

Supplementary data associated with this article can be found, in the online version, at <https://doi.org/10.1016/j.apcatb.2018.01.018>.

References

- [1] J. Schneider, M. Matsuoka, M. Takeuchi, J. Zhang, Y. Horiuchi, M. Anpo, D.W. Bahnemann, Understanding TiO_2 photocatalysis: mechanisms and materials, *Chem. Rev.* 114 (2014) 9919–9986.
- [2] C.T. Campbell, C.H. Peden, Oxygen vacancies and catalysis on ceria surfaces, *Science* 309 (2005) 713–714.
- [3] K. Zhao, L. Zhang, J. Wang, Q. Li, W. He, J.J. Yin, Surface structure-dependent molecular oxygen activation of BiOCl single-crystalline nanosheets, *J. Am. Chem. Soc.* 135 (2013) 15750–15753.
- [4] J. Lee, D.C. Sorescu, X.Y. Deng, Electron-induced dissociation of CO_2 on TiO_2 (110), *J. Am. Chem. Soc.* 133 (2011) 10066–10069.
- [5] H. Li, J. Shang, Z. Ai, L. Zhang, Efficient visible light nitrogen fixation with BiOBr nanosheets of oxygen vacancies on the exposed {001} facets, *J. Am. Chem. Soc.* 137 (2015) 6393–6399.
- [6] H. Li, J. Li, Z. Ai, F. Jia, L. Zhang, Oxygen vacancy-mediated photocatalysis of BiOCl: reactivity, selectivity and perspective, *Angew. Chem. Int. Ed.* 57 (2018) 122–138.
- [7] R. Schaub, P. Thostup, N. Lopez, E. Lægsgaard, I. Stensgaard, J.K. Nørskov, F. Besenbacher, Oxygen vacancies as active sites for water dissociation on rutile TiO_2 (110), *Phys. Rev. Lett.* 87 (2001) 266104.
- [8] H. Hussain, G. Tocci, T. Woolcot, X. Torrelles, C. Pang, D. Humphrey, C. Yim, D. Grinter, G. Cabailh, O. Bikondoa, Structure of a model TiO_2 photocatalytic interface, *Nature Mater.* 16 (2017) 461–466.
- [9] R. Schaub, E. Wahlström, A. Rönna, E. Lægsgaard, I. Stensgaard, F. Besenbacher, Oxygen-mediated diffusion of oxygen vacancies on the TiO_2 (110) surface, *Science* 299 (2003) 377–379.
- [10] M. Setvin, U. Aschauer, P. Scheiber, Y.-F. Li, W. Hou, M. Schmid, A. Selloni, U. Diebold, Reaction of O_2 with subsurface oxygen vacancies on TiO_2 anatase (101), *Science* 341 (2013) 988–991.
- [11] M. Setvin, J. Hulva, G.S. Parkinson, M. Schmid, U. Diebold, Electron transfer between anatase TiO_2 and an O_2 molecule directly observed by atomic force microscopy, *Proc. Natl. Acad. Sci. U. S. A.* 114 (2017) E2556–E2562.
- [12] U. Aschauer, J. Chen, A. Selloni, Peroxide and superoxide states of adsorbed O_2 on anatase TiO_2 (101) with subsurface defects, *Phys. Chem. Chem. Phys.* 12 (2010) 12956–12960.
- [13] H. Li, J. Shang, J. Shi, K. Zhao, L. Zhang, Facet-dependent solar ammonia synthesis of BiOCl nanosheets via a proton-assisted electron transfer pathway, *Nanoscale* 8 (2016) 1986–1993.
- [14] Y. Zhao, W. Ma, Y. Li, H. Ji, C. Chen, H. Zhu, J. Zhao, The Surface-structure sensitivity of dioxygen activation in the anatase-photocatalyzed oxidation reaction, *Angew. Chem. Int. Ed.* 51 (2012) 3188–3192.
- [15] J. Jiang, K. Zhao, X. Xiao, L. Zhang, Synthesis and facet-dependent photoreactivity of BiOCl single-crystalline nanosheets, *J. Am. Chem. Soc.* 134 (2012) 4473–4476.
- [16] L. Khachatryan, E. Vejerano, S. Lomnicki, B. Dellinger, Environmentally persistent free radicals (EPFRs). 1. Generation of reactive oxygen species in aqueous solutions, *Environ. Sci. Technol.* 45 (2011) 8559–8566.
- [17] Q. Kuang, X. Wang, Z. Jiang, Z. Xie, L. Zheng, High-energy-surface engineered metal oxide micro-and nanocrystallites and their applications, *Acc. Chem. Res.* 47 (2013) 308–318.
- [18] G. Pacchioni, Oxygen vacancy: the invisible agent on oxide surfaces, *ChemPhysChem* 4 (2003) 1041–1047.
- [19] M.V. Ganduglia-Pirovano, A. Hofmann, J. Sauer, Oxygen vacancies in transition metal and rare earth oxides: current state of understanding and remaining challenges, *Surf. Sci. Rep.* 62 (2007) 219–270.
- [20] L. Ye, L. Zan, L. Tian, T. Peng, J. Zhang, The {001} facets-dependent high photo-activity of BiOCl nanosheets, *Chem. Commun.* 47 (2011) 6951–6953.
- [21] H. Li, J. Shi, K. Zhao, L. Zhang, Sustainable molecular oxygen activation with oxygen vacancies on the {001} facets of BiOCl nanosheets under solar light, *Nanoscale* 6 (2014) 14168–14173.
- [22] Y. Wu, B. Yuan, M. Li, W.-H. Zhang, Y. Liu, C. Li, Well-defined BiOCl colloidal ultrathin nanosheets: synthesis, characterization, and application in photocatalytic aerobic oxidation of secondary amines, *Chem. Sci.* 6 (2015) 1873–1878.
- [23] F. Su, S.C. Mathew, L. Möhlmann, M. Antonietti, X. Wang, S. Blechert, Aerobic oxidative coupling of amines by carbon nitride photocatalysis with visible light, *Angew. Chem. Int. Ed.* 50 (2011) 657–660.
- [24] X. Lang, H. Ji, C. Chen, W. Ma, J. Zhao, Selective formation of imines by aerobic photocatalytic oxidation of amines on TiO_2 , *Angew. Chem. Int. Ed.* 50 (2011) 3934–3937.
- [25] J.P. Perdew, K. Burke, M. Ernzerhof, Generalized gradient approximation made simple, *Phys. Rev. Lett.* 77 (1996) 3865.
- [26] D. Vanderbilt, Soft self-consistent pseudopotentials in a generalized eigenvalue formalism, *Phys. Rev. B* 41 (1990) 7892.
- [27] G. Kresse, D. Joubert, From ultrasoft pseudopotentials to the projector augmented-wave method, *Phys. Rev. B* 59 (1999) 1758.
- [28] Y. Xu, M.A. Schoonen, The absolute energy positions of conduction and valence bands of selected semiconducting minerals, *Am. Mineral.* 85 (2000) 543–556.
- [29] A.L. Lazrus, G.L. Kok, S.N. Gitlin, J.A. Lind, S.E. McLaren, Automated fluorimetric method for hydrogen peroxide in atmospheric precipitation, *Anal. Chem.* 57 (1985) 917–922.
- [30] M. Tajbakhsh, R. Hosseinzadeh, H. Alinezhad, S. Ghahari, A. Heydari, S. Khaksar, Catalyst-free one-pot reductive alkylation of primary and secondary amines and N, N-dimethylation of amino acids using sodium borohydride in 2, 2, 2-trifluoroethanol, *Synthesis* 2011 (2011) 490–496.
- [31] K. Zhang, J. Liang, S. Wang, J. Liu, K. Ren, X. Zheng, H. Luo, Y. Peng, X. Zou, X. Bo, BiOCl sub-microcrystals induced by citric acid and their high photocatalytic activities, *Cryst. Growth Des.* 12 (2012) 793–803.
- [32] D. Ricci, C. Di Valentin, G. Pacchioni, P.V. Sushko, A.L. Shluger, E. Giamello, Paramagnetic defect centers at the MgO surface. An alternative model to oxygen vacancies, *J. Am. Chem. Soc.* 125 (2003) 738–747.
- [33] X. Chen, L. Liu, Y.Y. Peter, S.S. Mao, Increasing solar absorption for photocatalysis with black hydrogenated titanium dioxide nanocrystals, *Science* 331 (2011) 746–750.
- [34] Z. Lin, J. Li, Z. Zheng, J. Yan, P. Liu, C. Wang, G. Yang, Electronic reconstruction of $\alpha\text{-Ag}_2\text{WO}_4$ nanorods for visible-light photocatalysis, *ACS Nano* 9 (2015) 7256–7265.
- [35] L. Liu, Y.Y. Peter, X. Chen, S.S. Mao, D. Shen, Hydrogenation and disorder in engineered black TiO_2 , *Phys. Rev. Lett.* 111 (2013) 065505.
- [36] L. Vaska, Dioxygen-metal complexes: toward a unified view, *Acc. Chem. Res.* 9 (1976) 175–183.
- [37] H. Tong, S. Ouyang, Y. Bi, N. Umezawa, M. Oshikiri, J. Ye, Nano-photocatalytic materials: possibilities and challenges, *Adv. Mater.* 24 (2012) 229–251.
- [38] X. Xiao, J. Jiang, L. Zhang, Selective oxidation of benzyl alcohol into benzaldehyde over semiconductors under visible light: the case of $\text{Bi}_{12}\text{O}_{17}\text{Cl}_2$ nanobelts, *Appl. Catal. B-Environ.* 142 (2013) 487–493.
- [39] M.A. Fox, M.J. Chen, Photocatalytic formylation of primary and secondary amines on irradiated semiconductor powders, *J. Am. Chem. Soc.* 105 (1983) 4497–4499.
- [40] P. Rieger, Electron Spin Resonance: Analysis and Interpretation, RSC, Cambridge, 2007, pp. 4–5.
- [41] S. Furukawa, Y. Ohno, T. Shishido, K. Teramura, T. Tanaka, Selective amine oxidation using Nb_2O_5 photocatalyst and O_2 , *ACS Catal.* 1 (2011) 1150–1153.
- [42] X.J. Yang, B. Chen, X.B. Li, L.Q. Zheng, L.Z. Wu, C.H. Tung, Photocatalytic organic transformation by layered double hydroxides: highly efficient and selective oxidation of primary aromatic amines to their imines under ambient aerobic conditions, *Chem. Comm.* 50 (2014) 6664–6667.
- [43] N. Zhang, X. Li, H. Ye, S. Chen, H. Ju, D. Liu, Y. Lin, W. Ye, C. Wang, Q. Xu, Oxide defect engineering enables to couple solar energy into oxygen activation, *J. Am. Chem. Soc.* 138 (2016) 8928–8935.
- [44] C. Hansch, A. Leo, R. Taft, A survey of Hammett substituent constants and resonance and field parameters, *Chem. Rev.* 91 (1991) 165–195.
- [45] H.C. Brown, Y. Okamoto, Electrophilic substituent constants, *J. Am. Chem. Soc.* 80 (1958) 4979–4987.
- [46] B. Barbier, J. Pinson, G. Desarmot, M. Sanchez, Electrochemical bonding of amines to carbon fiber surfaces toward improved carbon-epoxy composites, *J. Electrochem. Soc.* 137 (1990) 1757–1764.
- [47] M. Xing, J. Zhang, F. Chen, B. Tian, An economic method to prepare vacuum activated photocatalysts with high photo-activities and photosensitivities, *Chem. Comm.* 47 (2011) 4947–4949.
- [48] R. Makkay, M. Fine, Vacuum reduction of $\alpha\text{-Nb}_2\text{O}_5$ at low temperatures, *J. Appl. Phys.* 33 (1962) 745.